Answer to Referee #1

Page 1347, line 24: The word volume has been deleted. We derive the extinction coefficient and not the volume extinction coefficient

Page 1348, line 13: the sentence has been changed as proposed by the reviewer:

'The lidar measurement site at South Africa was located on a hill top at Elandsfontein (26°15´S, 29°26´ E, 1745 m a.s.l.) in the Highveld region.'

Page 1350, line 18: The word 'campaigns' has been replaced by the word 'campaign'

Page 1351, line 2: The phrase 'are derived' has been replaced by the phrase 'is derived'

Page 1352, line 27: The percentage is relative to the number of possible measurement. The sentence has been changed accordingly: 'In Figure 1(b) we present the percentage of the measurements in which at least one free-tropospheric aerosol layer was observed (green bars) relative to the hourly averaged (every three hours) lidar measurements.'

Figure 2: The height of the PBL top was continuously measured by Polly^{XT} lidar. The results were presented by Korhonen et al., 2014. The lower geometrical bottom of the aerosol layers presented in this study (Figure 3) is around 500 m. In order to clarify that the PBL height is lower than the bottom of the layers we present the hourly PBL height as well as the difference between the bottom of the first free tropospheric layer observed and the PBL.
The variability of PBL is shortly discussed in the new manuscript.
'South Africa is a region of high atmospheric variability on both short-scale (days to weeks) and seasonal time spans. This atmospheric variability together with a large surface temperature range and significant seasonal changes in precipitation has an impact on the vertical mixing of particulate matter, and hence, on the PBL evolution'
A reference is also given for more details. The diurnal cycle of PBL observed in Elandsfontein during 2010 was discussed in detail and presented by Korhonen et al., 2014.

Page 1354, line 15 : In this study we first derived the layer properties of the individual 1-hour profiles and then average on monthly basis. The sentence has been changed accordingly: 'The analyzed hourly center height, geometrical depth and AOD at 355 and 532 nm are monthly averaged and presented in Figure 4 (a), (b) and (c) respectively.'

Figure 6: Caption on Figure 6 has changed as proposed by the reviewer: 'Variation of AOD at 355 nm (a) of the boundary layer (blue squares) and the free troposphere (orange circles) and (b) the monthly free tropospheric contribution to total AOD at 355 nm. In (b) the squares represent the mean value, the horizontal line the median, the boxes the 25 and 75 % percentiles, the whiskers the standard deviation and the stars the maximum and minimum values during the respective month.'

Answer on the general comment on sections 3.1 and 3.2:

In this paper we present the statistics on the seasonal behavior of free tropospheric aerosol layers above South Africa. Our initial aim was to attribute each aerosol layer to a certain aerosol type, since

different source regions emit different kinds of aerosol. However, this was not possible because the aerosol layers were often observed in a mixing state rather than as one single pure aerosol type. In this study we present the statistics on the seasonal behavior of free tropospheric aerosol layers above South Africa. Detailed analysis with respect to optical and microphysical aerosol properties for selected aerosol layers that have been assigned to specific aerosol types will be followed up in a subsequent article.

Answer to Referee #2

Comment on aerosol optical depth at 532 and Ångström related to backscatter (355 – 532 nm)

We retrieve the aerosol optical depth at 532 on 163 cases, which is more than the half of the measurement cases comparing with the aerosol optical depth at 355 nm. The seasonally behaviour of aerosol optical depth, as shown in Figure 4, is the same for both wavelengths. Also, in Figure 5 the aerosol optical depth at 532 is very well compared to sunphotometer values, taking into account that Raman lidar measurements are performed only night time while sunphotometer data are referring to daytime measurements along with the fact that our site face strong diurnal variation regarding the aerosol load.

In addition, the Ångström related to backscatter values between 355 and 532 (as well as the Ångström related to backscatter values between 532 and 1064 nm) are already given to the Table 3 for each of the seasons as well as for the dry, wet and biomass burning period.

Comment on aerosol typing:

In this paper we present the statistics on the seasonal behavior of free tropospheric aerosol layers above South Africa. Our initial aim was to attribute each aerosol layer to a certain aerosol type, since different source regions emit different kinds of aerosol. However, this was not possible because the aerosol layers were often observed in a mixing state rather than as one single pure aerosol type. In this study we present the statistics on the seasonal behavior of free tropospheric aerosol layers above South Africa. Detailed analysis with respect to optical and microphysical aerosol properties for selected aerosol layers that have been assigned to specific aerosol types will be followed up in a subsequent article.

Comment on depolarization

The particle depolarization ratio at 355 nm has not been retrieved for the aerosol optical profiles that has been analyzed in this paper. As mentioned previously a second paper will follow, discussing the optical (also depolarization) and microphysical aerosol properties on selected case studies. The analysis on the selected cases has shown that depolarization is less than 5 % on the majority of the cases, while some biomass burning aerosol layers appears with depolarization ratios as much as 10%. There is no indication of desert dust aerosol layers in our study.

Comment about errors in the retrieval of optical properties:

A paragraph concerning the error in the optical properties has been added in Section 2.1

'The relative errors in the nighttime aerosol products are mainly determined by signal noise. Systematic uncertainties introduced by the correction of Rayleigh scattering, air density, and overlap effects are of the order of 5%-10% for heights above 500 m. The overall relative errors of the lidar-derived aerosol

properties are in the range of 5%-15% for backscatter coefficients, 10%-30% for extinction coefficients, 15%-40% for lidar ratios and about 5%-10% for AODs (Ansmann et al., 1992; Hänel et al., 2012). ‘

Page 10, end of Section 3

In the end of section 3 there is no discussion relatively to the first idea.

Section 4.2

The number of the layers averaged is given in the Tables 1,2 and 3. The number of layers is more than 40 except for the retrieval of extinction at 532 during summer which is 18 layers (this mean 28% of the layers observed during summer).

Comment regarding Figure 7-9-10

Figure 7 presents the monthly variation of wind speed and the number of hotspots. The frequency sum of all parameters given in Figures 8,9 and 10 is 100%. The number given in each column is the number of atmospheric layers found in each bin group (and not the % percententage). The percentages are given in Y-axis. This is now clarified in the figure captions.

One year of Raman lidar observations of free tropospheric aerosol layers over South Africa

E. Giannakaki[1], A. Pfüller[1], K. Korhonen[1,2], T. Mielonen[1], L. Laakso[3,4], V. Vakkari[3], H. Baars[5], R. Engelmann[5], J. P. Beukes[4], P. G. Van Zyl[4], M. Josipovic[4], P. Tiitta[4,6], K. Chiloane[7], S. Piketh[4], H. Lihavainen[3], K.E.J. Lehtinen[1,2] and M. Komppula[1]

(1){Finnish Meteorological Institute, P.O.Box 1627, FI-70211, Kuopio, Finland}

(2){Department of Applied Physics, University of Eastern Finland, P.O. BOX 1627, FI-70211 Kuopio, Finland}

(3){Finnish Meteorological Institute, P.O.Box 503, FI-00101, Helsinki, Finland}

(4){Unit for Environmental Sciences and Management, North-West University, Potchefstroom, South Africa}

(5){Leibniz Institute for Tropospheric Research, Permoserstrasse 15, D-04318, Leipzig, Germany}

(6){Department of Environmental Sciences, University of Eastern Finland, P.O. BOX 1627, FI-70211 Kuopio, Finland}

(7){Eskom Holdings SOC Ltd, Sustainability Division; Research, Testing and Development, South Africa}

Correspondence to: Elina Giannakaki (Eleni.giannakaki@fmi.fi)

Field Code Changed

Abstract

Raman lidar data obtained over a one year period has been analyzed in relation to aerosol layers in the free troposphere over the Highveld in South Africa. In total, 375 layers were observed above the boundary layer during the period 30 January 2010 – 31 January 2011. The seasonal behavior of aerosol layer geometrical characteristics, as well as intensive and extensive optical properties were studied. The highest center heights of free tropospheric layers were observed during the South African spring (2520 ± 970 m ~~above ground level (A.G.L.)~~ a.g.l., also elsewhere). The geometrical layer depth was found to be maximum during spring, while it did not show any significant difference for the rest of the seasons. The variability of the analyzed intensive and extensive optical properties was high during all seasons. ~~This was attributed to the mixing state of aerosols and the different transport paths of the aerosol layers.~~ Layers were observed at a mean center ~~altitude~~ height of 2100 ± 1000 m ~~A.G.L.~~ with an average lidar ratio of 67 ± 25 sr (mean value with one standard deviation) at 355 nm and a mean extinction-related Ångström exponent of 1.9 ± 0.8 between 355 and 532 nm during the period under study. Except for the intensive biomass burning period from August to October, the lidar ratios and Ångström exponents are within the range of previous observations for urban/industrial aerosols. During southern hemispheric spring, the biomass burning activity is clearly reflected in the optical properties of the observed free tropospheric layers. Specifically, lidar ratios at 355 nm were 89 ± 21 sr, 57 ± 20 sr, 59 ± 22 sr~~65 ± 23 sr~~, ~~59 ± 22 sr~~ and 65 ± 23 sr ~~89 ± 21 sr~~ during spring (September – November), summer (December – February), autumn (March – May) ~~winter (June – August), autumn (March – May)~~ and winter (June – August) ~~spring (September – November)~~, respectively. The extinction-related Ångström exponents between 355 and 532 nm measured during

spring, summer, ~~winter,~~ autumn and winter ~~spring~~ were 1.8 ± 0.6, 2.4 ± 0.9, ~~1.8 ± 0.6,~~ 1.8 ± 0.9 and 1.8 ± 0.6, respectively. The mean columnar aerosol optical depth (AOD) obtained from lidar measurements was found to be 0.46 ± 0.35 at 355 nm and 0.25 ± 0.2 at 532 nm. The contribution of free tropospheric aerosols on the AOD had a wide range of values with a mean contribution of 46%.

1. Introduction

Atmospheric aerosols of natural and anthropogenic origin contribute substantially to global climate variability (IPCC, 2013). A detailed understanding of the regional geometrical characteristics and optical properties of aerosols, as well as their temporal and spatial distribution is required before we can accurately evaluate aerosol effects in the climate system (Hsu et al., 2000). However, high-quality aerosol measurements in the southern hemisphere are rather limited. South Africa is located at the southernmost tip of the African continent, extending from 22^{o}S to 34^{o}S latitude and from 16^{o}E to 32^{o}E longitude. Previous studies have indicated that South Africa is one of the most affected countries in the world with regard to aerosol load, due to various natural and anthropogenic activities (Piketh et al., 2000; Piketh et al., 2002; Formenti et al., 2002, 2003; Campbell et al., 2003; Eck et al., 2003; Freiman and Piketh, 2003; Ichoku et al., 2003; Ross et al., 2003; Winkler et al., 2008; Queface et al., 2011; Tesfaye et al., 2011; Venter et al., 2012; Tiitta et al., 2014).

According to Giglio et al. (2010), 70% of the total area burned worldwide annually occurs in Africa. In order to assess the influence of wildfire aerosols on the climate system, it is important to know their altitude distribution. If wildfire aerosols are for example involved in cloud activation processes, it can alter cloud development through indirect and semi-direct aerosol effects (Ramanathan et al., 2001; Andreae et al., 2004; Koren et al., 2004; Koren et al., 2008; Rosenfeld et al., 2008). In addition, vertical transport can change the residence time and horizontal transport patterns of the absorbing aerosols. Vakkari et al. (2014) also recently showed that in biomass burning plumes in South Africa secondary aerosol formation increases significantly the aerosol mass and number concentrations during plume transport.

79 The Southern Hemisphere is relatively devoid of major dust activity (Prospero et al.,
80 2002). In southern Africa one source of mineral dust is located in Botswana in the
81 region centered at 21^{o}S, 26^{o}E with highly variable activity from year to year, while a
82 second small but persistent source is centered at 16^{o}E, 18^{o}S over the Etosha Pan, an
83 extremely flat salt pan in northern Namibia (Prospero et al., 2002; Bryant et al., 2007).
84 Robles-Gonzalez and Leeuw (2008) have measured AODs of up to 0.75 at 555 nm
85 over Namibian and Kalahari deserts during SAFARI-2000.
86 Long-term studies of atmospheric aerosols over the continental Southern Hemisphere
87 are limited. In general, previous studies pointed out the importance of regional
88 circulation and seasonal pollutant variation. In these long-term investigations the
89 optical properties of aerosols have been studied by means of sun photometers (e.g.
90 Queface et al., 2011), *in situ* data (e.g. Laakso et al., 2012) and satellite observations
91 (e.g. Tesfaye et al., 2011). Sun photometers provide column optical properties from
92 which microphysical information can be deduced. Although *in situ* surface
93 observations provide detailed optical, chemical and microphysical characterization of
94 particles, they are often point measurements. Optical properties of boundary layer
95 aerosols that originate from local sources and regionally transported aerosols are
96 usually different from free tropospheric aerosols that generally originate from long-
97 range transport.
98 Considering the above mentioned, there is a clear need for vertically resolved
99 observations with advanced multiwavelength lidars. Lidar systems provide vertical
100 profiles of atmospheric aerosols with a high temporal and spatial resolution. They are
101 powerful tools for the geometrical characterization of free tropospheric aerosols (e.g.
102 Mattis et al., 2008) and for the analysis of aerosol optical properties (e.g. Müller et al.,
103 2007), which are the key factors in determining the impact of aerosols on solar

radiation (Wagner et al., 2001). The optical characterization of aerosols is made possible with the independent detection of particle extinction and backscattering properties by the use of the Raman-lidar technique (Ansmann et al., 1992). Modern lidars are able to measure ~~volume~~aerosol extinction coefficient profiles at two wavelengths and therefore determine the extinction-related Ångström exponent (Ångström, 1964), which contains information on particle size. Numerous studies (e.g. Ansmann et al., 2002; Müller et al., 2007; Groß et al. 2013; Mona et al., 2006) have demonstrated that the lidar ratio (i.e. extinction-to-backscatter ratio) is a valuable parameter for aerosol characterization since it depends on the particles microphysical and chemical properties and therefore varies significantly for different aerosol types. Based on 10 years of lidar observations around the globe, intensive optical properties of several aerosol types were presented by Müller et al. (2007). However, long-term lidar studies often reveal high variability in the optical properties measured (Balis et al., 2004; Papayannis et al. 2008; Amiridis et al., 2009; Giannakaki et al., 2010, Hänel et al., 2012; Komppula et al. 2012; Baars et al. 2012) due to the high temporal and spatial variability of the aerosol occurrences.

The measurements presented in this paper were performed within the framework of the EUCAARI project (Kulmala et al., 2011). Four key regions outside Europe were chosen to perform at least one year of Raman lidar measurements for greater insight into aerosol effects on global climate. Apart from the South African measurements (Laakso et al., 2012), measurements took place in the Amazon Basin (Baars, 2012), India (Komppula, 2012) and China (Hänel, 2012).

The lidar measurement site at South Africa was located on a hill top at Elandsfontein (26^{o}15´S, 29^{o}26´ E, 1745 m a.s.l.) in the Highveld region ~~of South Africa~~. The station was located approximately 150 km east from the Johannesburg-Pretoria megacity,

which is the largest metropolitan area in South Africa with a population of over 10 million people (Lourens et al., 2012).

One significant source of atmospheric pollutants in the region is biomass burning through wild and agricultural fires (Tummon et al., 2010; Swap et al., 2003). In addition, the burning of solid fuels such as wood, dung and residual crops for domestic cooking and ~~space~~ heating is also an important source of emissions into the atmosphere in southern Africa. These emissions (from wild fires and domestic burning), when transported above boundary layer, are difficult to distinguish from one to another. Marufu et al. (2000) have estimated that household emissions account for at least ~~as much as~~ wild fire burning and industrial emissions. Another source of aerosols in the ~~region~~ investigated region is ~~anthropogenic emissions~~pollution from industrialized regions in South Africa. The major industrial pollution sources within a 50 km radius of the measurement site include ten coal-fired power plants, a petrochemical plant and some metallurgical plants (Laakso et al., 2012). Desert dust aerosols emitted from Botswana and Namibia deserts might be also possible sources of aerosols in this region. The short~~est~~ distance ~~to~~ from the Indian Ocean is approximately 350 km, therefore marine air masses can also have an impact on atmospheric aerosols at Elandsfontein.

A dominant characteristic of the South African Highveld climate is the variation between wet (October to March) and dry (April to September) periods. Approximately 90% of the annual precipitation falls during the wet period. The limited cloud cover during the dry season results in strong nocturnal inversions and reduced vertical mixing at night-time (Laakso et al., 2012), while during daytime strong surface heating and thus vertical mixing occurs. In contrast, the cloudiness and precipitation increase dramatically during the rainy season.

There are variations in the definition of climatic seasons in South Africa since South Africa does not really experience four distinct seasons. According to actual weather conditions, spring can be rather short, lasting only two months, while the summer is usually relatively long. In this study we accept the definition used in Tyson, P.D. and Preston-Whyte, R.A (2004):. ~~Each~~ each season lasts for a period of three months with summer being from December to February, autumn from March to May, winter from June to August and spring from September to November. In addition, we present statistical results for the wet and dry periods, as well as for the "intense" biomass burning period (August to October).

In this study we summarize one year of Raman lidar observations over South Africa. The analyses of lidar measurements presented here could assist in bridging existing gaps on the knowledge of vertical distribution of aerosols above South Africa, since limited long-term data of this type is available for this region. For the first time, we have been able to cover the full seasonal cycle ~~on~~ of geometrical characteristics and optical properties of free tropospheric aerosol layers in the region.

A description of the instrumentation and the data processing used in this study is presented in Sect. 2. The geometrical characteristics and AOD of free tropospheric aerosol layers as well as the intensive and extensive optical properties of the layers are discussed in Sect. 3. The paper ends with a summary and conclusions in Sect. 4.

2. Instrumentation and methodology

2.1. Multi-wavelength Raman lidar

A multi-wavelength Raman lidar Polly^{XT} (Althausen et al., 2009) supplied by the Finnish Meteorological Institute (FMI) was operated remotely at Elandsfontain in South Africa. Polly^{XT} works with a Nd:YAG laser emitting at its primary wavelength

of 1064 nm, which, after ~~frequency~~ doubling and tripling the frequency, emits at the wavelengths of 532 and 355 nm, respectively. The receiver consists of a Newtonian telescope with a diameter of 300 mm and a field of view of 1 mrad. Photomultiplier tubes (PMT) are used for the detection of the elastically backscattered photons at 355, 532 and 1064 nm, as well as the in-elastically backscattered photons at 387 and 607 nm that corresponds to the Raman-shift by ~~nitrogen~~ Nitrogen molecules at 355 and 532 nm, respectively. Additionally, the cross polarized component at 355 nm is detected ~~that~~ for ~~consequently allows~~ the determination of the linear particle depolarization ratio. The vertical resolution is 30 m and the raw data is typically stored as average values calculated over 30 s. Data was collected on the web page of PollyNet (http://polly.tropos.de) where the "quicklooks" of all measurements are available.

Field Code Changed

The relative errors in the nighttime aerosol products are mainly determined by signal noise. Systematic uncertainties introduced by the correction of Rayleigh scattering, air density, and overlap effects are of the order of 5%-10% for heights above 500 m. The overall relative errors of the lidar-derived aerosol properties are in the range of 5%-15% for backscatter coefficients, 10%-30% for extinction coefficients, 15%-40% for lidar ratios and about 5%-10% for AODs (Ansmann et al., 1992; Hänel et al., 2012).

The Polly^{XT} of FMI had also been deployed in a long-term aerosol experimental campaign~~s~~ at Gual Pahari, India (March 2008 – March 2009) (Komppula et al., 2012) and is currently operating at Vehmasmäki, Finland (62°44'17" N, 27°32'33.5" E, 190 m a.s.l.). The lidar system has been recently upgraded (Engelmann et al., 2012) and is now part of the European Aerosol Research Lidar Network (EARLINET) (Bösenberg

et al., 2003; Pappalardo, et al., 2014) and the Finnish lidar network (Hirsikko et al., 2014).

2.2. Auxiliary data

Moderate Resolution Imaging Spectroradiometer (MODIS) collection 5 active fire product data was used in this study to determine the number of wild fire hotspots in the region (Roy et al., 2008). Hotspots is a satellite data product that has been widely used for mapping fire occurrence and is~~are~~ derived from temperature anomalies registered by the middle and thermal infrared sensors (Hantson et al., 2012).

Basic meteorological parameters were measured with a Vaisala WXT510 meteorological station (Vaisala, WXT510 specification sheet, 2010) at the site. Measurements included wind direction and ~~-~~speed with an acoustic anemometer, as well as temperature, relative humidity and rain density (Laakso et al., 2012).

2.3. Lidar data evaluation

Lidar measurements ~~commenced~~ started on 11 December 2009 and were ~~conducted~~ ~~up~~performed until 31 January 2011. The measurements were carried out continuously, with the exception of two periods during which maintenance was performed, i.e. from 23rd December 2009 to 26th January 2010 and from 23rd October 2010 to 23rd November 2010. Polly^{XT} collected measurements on 310 days for a total of 4935 h. In order to determine the optical profiles, the data was hourly averaged every three hours, i.e. leaving a gap of two hours between individual averaged measurements, when the atmospheric conditions were homogeneous and free of low and medium height clouds. The detection of low or medium height clouds was based on the range corrected signal which gets totally attenuated within the first height bins above the cloud base. ~~-~~Only night-time measurements are analyzed in this study since Raman signals are too weak to be detected with the Polly^{XT} during daytime. The main

objective is to study the extensive (backscatter and extinction coefficients) and intensive (lidar ratio, Ångström exponents) optical properties of free tropospheric aerosol layers in the region. The extinction and the backscatter coefficient profiles at 355 and 532 nm have been obtained with the Raman method (Ansmann et al., 1992), while the backscatter at 1064 nm has been determined using the Klett method (Klett, 1981). An overlap correction has been applied on the basis of a simple technique proposed by Wandinger and Ansmann (2002). The depolarization ratio profiles are not analyzed in this study.

The range-resolved elastic backscatter signal contains information that can be used to derive the height of aerosol layers. The gradient method~~, also used in the EARLINET community,~~ was applied to determine the bottom and top layer heights of the aerosols in the free troposphere (Flamant et al., 1997; Bösenberg et al., 2003; Mattis et al., 2008). In general, the local maximum in the first derivative of backscatter at 1064 nm is considered to be the bottom of a layer, while the local minimum is considered to be the top of the layer. In order to verify the gradient method, we checked whether the layer boundaries identified by the gradient method coincide with the bottom and top heights that we recognize in coherent structures of the height time displays of the range-corrected lidar signal.

In this work we analyzed the geometrical characteristics of the free tropospheric aerosol layers above the measurement site. Layers observed inside the boundary layer are not analyzed in this study. ~~This involved determining t~~The top of the planetary boundary layer was determined as presented by Korhonen et al. (2014). Planetary boundary layer top heights were retrieved from the lidar backscatter signal at 1064 nm using the Wavelet Covariance Transform method (Brooks, 2003). The accuracy on geometrical boundaries identification of free tropospheric aerosol layers depends on

the correct determination of PBL top height. Korhonen et al. (2014) have shown that the Wavelet Covatiance Transform method performs well despite the frequent complex vertical aerosol layer structures caused by large emissions from large point sources and biomass burning. Subsequently, 7-day back-trajectories were calculated by means of the HYSPLIT model (Draxler and Hess, 1997; Draxler and Hess 1998) for the center height of each elevated layer.

3. Results and discussion

The percentage of the night-time measurements performed each month in terms of hourly averaged profiles every three hours (i.e. leaving a gap of two hours between individual averaged measurements) is presented in Figure 1(a) (blue bars), which varies between 3 and 72 % for all the months. The percentage was calculated by taking into account the night time hours for each month. Analysis could not be performed during unfavorable weather conditions, such as the presence of low clouds and rain (shaded bars) or due to the scheduled shutdowns (grey bars). In Figure 1(b) we present the percentage of the measurements in which at least one free-tropospheric aerosol layer was observed (green bars) relative to the hourly averaged (every three hours) lidar measurements. The total number of the observed free-tropospheric layers per month is presented with red stars in the same figure. In total, 375 aerosol layers were observed above the boundary layer during the period studied.

In this region, approximately 90% of the annual precipitation falls during the wet season (October - March) (Laakso et al., 2012 and references therein), as indicated in Figure 1 (c). Fewer measurements were performed during the wet period. The seasonal precipitation cycle should not only affect the number of measurements that could be performed but also the total number of layers observed. Therefore it is

expected that the fraction of measurements of free-tropospheric aerosol layers in relation to the total number of observations should be less during the wet season due to wet scavenging. However, our results indicate that during the wet period a relatively large number of layers are still observed in the free troposphere. The general anticyclonic nature of atmospheric circulation over the region, results in the formation of absolutely stable layers of air throughout the year (Cosijn and Tyson, 1996). According to the same study the absolutely stable air layers occur preferentially at around the 700, 500 and 300 hPa levels and are spatially extensive and temporally persistent in fair weather conditions.

3.1. Geometrical characteristics and optical depth of free tropospheric aerosol layers

In order to define the geometrical boundaries of free tropospheric aerosol layers we need to dermine the PBL top height. In this study the determination of PBL top height was performed for the hourly night-time lidar observations and only for the cases which at least one layer was observed. The PBL top height is presented in Figure 2(a). The average PBL top height was found to be 1440 ± 656 m A.G.L. The highest PBL top height was observed during spring (October) while lower PBL values were observed in winter. South Africa is a region of high atmospheric variability on both short-scale (days to weeks) and seasonal time spans. This atmospheric variability together with a large surface temperature range and significant seasonal changes in precipitation has an impact on the vertical mixing of particulate matter, and hence, on the high variability of PBL top height as shown in Figure 2. The diurnal cycle of PBL observed in Elandsfontein during 2010 is presented in detail by Korhonen et al., 2014. The difference between the bottom of the first free tropospheric aerosol layer observed from the PBL height is presented in Figure 2(b). Forty five percent (45%) of

Formatted: English (U.S.)

Formatted: English (U.S.)

Formatted: English (U.S.)

Formatted: English (U.S.)

Formatted: English (U.S.)

the elevated layers were separated by up to 500 m from the PBL aerosols. In about of 20% of the hourly analyzed cases the free tropospheric layers were separated by more than 1000 m from the PBL height.

Figure 3 shows our complete data set of lidar measurements in terms of geometrical characteristics. The vertical lines present the observed height ranges of free tropospheric aerosol layers. Out of 429 hourly analyzed lidar observation, we observe free tropospheric ~~pollution events~~aerosol layers on 223 hourly analyzed observations (i.e. 52 %). In total 375 free tropospheric aerosol layers were observed. ~~Pollution events~~The free-tropospheric aerosol layers are observed as a single layer on 52% of the cases, while they are often characterized by two (32 %), three (13 %) or more particle layers (3%). Up to five layers were observed simultaneous. The maximum top height observed was 5730 m A.G.L. on 22 August 2010, while the minimum bottom height was 400 m A.G.L. and observed on 21 of July 2010. The geometrical depth of the free tropospheric layers varies from a few hundred meters to several kilometers throughout the period under investigation. Figure 3 already indicates that layers are observed at higher elevation levels during the second half of the year.

~~Monthly averaged lidar measurements analyzed in terms~~The analyzed hourly center height, geometrical depth and AOD at 355 and 532 nm are monthly averaged and presented in Figure 4 (a), (b) and (c) respectively ~~of center height (a), geometrical depth (b), and AODs (c) at 355 and 532 nm for the period investigated are presented in Figure 4~~. The AOD measured is the integrated extinction coefficients at 355 and 532 nm for each layer identified. From the total number of free-tropospheric layers observed, 72% occurred at heights higher than 1500 m A.G.L. The higher and thicker layers were observed during the second half of the year. According to the MODIS fire product in year 2010 the biomass burning activity started in July and lasted until

October (https://firms.modaps.eosdis.nasa.gov/animations/2010_animation.gif), which is a typical seasonal pattern in southern Africa (e.g. Ito et al., 2007). The increase in biomass burning activity most probably contributes to higher and more frequent aerosol layer observations from August to October. During winter a surface inversion layer extends from the ground up to 300 m above the surface. An absolutely stable layer at 3000 m, above sea level is also present in 90% of days during winter (Cosijn and Tyson, 1996). The effective height of the power station stacks are around 400 m (http://www.eskom.co.za). So, during winter nights aerosol layer plumes can be trapped between the surface layer and the absolutely stable layer.

Due to low signal-to-noise ratios, analysis of the optical properties could not be performed for the entire dataset. For this reason the number of geometrically observed layers (Fig. 4a) is larger (or equal) than the number of layers for which layer AOD could be calculated (squares in Figure 4(c)). Mean extinction coefficient and thus layer AOD show large variations both at 355 and 532 nm. On average, aerosol layer optical depths at both wavelengths were below 0.1. Only during late winter and spring the mean AOD of free tropospheric layers at 355 nm was above 0.1. Maximum values of layer AOD ~~of~~ up to 0.3 at both wavelengths were reached, which is a significant (in the order of 85%) contribution to the columnar AOD. During May and June large extinction coefficients are observed for the lower layers.~~The larger extinction coefficients at both wavelengths during May and June are observed for lower layers.~~ However, the corresponding AODs are low due to small geometrical depths of these layers.

In order to further investigate the contribution of the free tropospheric aerosol load to the columnar AOD we studied the columnar, free tropospheric and boundary layer AODs in more detail. For each of the lidar measurements analyzed, columnar AOD

Field Code Changed

estimates were determined by integrating the aerosol extinction coefficient at 355 nm and 532 nm. We assumed that the extinction value at the height for which the overlap function is equal to 0.7 is representative down to the surface to account for the incomplete overlap region. The value of 0.7 is reached between 300 and 500 m. Therefore, this is a reasonable assumption and it is also a common approach in lidar studies (e.g. Giannakaki et al., 2010). In Figure 5 we present the columnar AOD calculated from each of the hourly analyzed lidar measurements at 355 (a) and 532 nm (b). In the same figure sun photometer daily values are presented for 340 and 380 nm (a) as well as for 500 nm (b).The mean columnar AOD obtained from lidar measurements was found to be 0.46 ± 0.35 at 355 nm and 0.25 ± 0.2 at 532 nm. The direct comparison of the two datasets is not the purpose of this study since sun photometer values are referring to day time measurements while lidar data are night-time measurements. The lidar derived columnar AOD exhibits a seasonal variability, with maximum values of 1.54 and 0.78 at 355 and 532 nm, respectively, measured in late September. The same seasonal behavior is also observed with sun photometer.

In an effort to explain the observed seasonality of the columnar AOD, we separately estimated the AOD in the boundary layer and the free troposphere at 355 nm, which are presented in Figure 6 (a). As can be seen in Figure 6 (a), the same seasonal pattern is observed for the AOD at 355 nm in the boundary layer and the free troposphere, i.e. larger AOD values are measured during late July, August, September and October in the boundary layer and the free troposphere. This is also found for the AOD at 532 nm (not shown here). In Figure 6 (b) we present the percentage contribution of free tropospheric AOD to the total AOD. Large variations of the contribution of free tropospheric AOD to the total AOD are observed for the period investigated, with a mean value of 46%. The largest monthly contribution of 58% is observed in October.

The period with increases in columnar, free tropospheric and boundary layer AODs coincides with higher wind speeds as presented in Figure 7(a) and an increase in biomass burning activity in South Africa shown in Figure 7(b). Tesfaye et al. (2011) attributed the increase of columnar AODs mainly to local sources and enhanced wind speeds. Higher wind speeds could lead to an increased transport of biomass emissions from regions further away from Elandsfontein. The increase in biomass burning activity in South Africa also contributes to enhance free tropospheric AOD. This is supported by the higher altitude of the observed aerosol layers during August, September and October (Figure 3). The number of hotspots (http://earthdata.nasa.gov/data/nrt-data/firms/active-fire-data) that was observed in the latitude range between 40°S and 20°S and longitude range between 20°E and 40°E degrees are plotted in Figure 7 (b). The results are presented in two clusters of medium (30-80%) and high confidence (80-100%) (https://earthdata.nasa.gov/data/near-real-time-data/firms/about). The number of hotspots with high confidence, in the region under study, ranges from 10000 to 15000 during August, September and October; while it is less than 2000 for the rest of the months.

Field Code Changed

Histograms of the geometrical center height of the lofted~~elevated~~ particle plumes with bin intervals of 750 m are shown in Figure 8 for each of the seasons. In the same figure, the statistical distribution for each season is also presented with box and whisker plots. High variation in the geometrical characteristics is observed throughout the year. Mean values of geometrical centers, as well as AODs at 355 and 532 nm are presented in Table 1. In general, free tropospheric aerosol layers were found at higher altitudes in spring and summer. The peak of the frequency distribution of the geometrical mean height of the observed free-tropospheric aerosol layers during

spring and summer were found to be between 2250 and 3000 m A.G.L., while for autumn and winter the peak ranges between 1500 and 2250 m A.G.L. Only 35% of the analyzed free tropospheric aerosol layers were observed below 2250 m A.G.L. during spring, while in summer, autumn and winter 43, 74, and 75 % of the free tropospheric aerosol layers were observed below 2250 m, respectively. The higher free tropospheric aerosol layers during spring is possibly due to intensive biomass burning activity in central and southern Africa and the transport of smoke above our measurement site. Seven-days back-trajectories analysis together with superimposed hotspots derived by MODIS for each of the layers identified reveals long range transport of biomass burning aerosols over Elandsfontein in most of the cases analyzed during spring.

3.2. Extensive and intensive optical properties of free tropospheric aerosol layers

Detailed statistical information on the extensive aerosol properties is presented in Table 2. It is evident that a wide range of extinction and backscatter coefficients for the four seasons during the year is observed. In addition to seasonal values we also present the values for wet, dry and biomass burning periods.

Mean Ångström exponents and lidar ratios were derived for the observed geometrical layers in cases that the extinction and backscatter coefficients profiles could be obtained. The monthly averaged lidar ratio at 355 and 532 nm, as well as the Ångström exponents of free tropospheric layers are presented in Figure 9.

Between late winter and throughout spring high lidar ratios are observed at both wavelengths. During this period a significant number~~contribution~~ of aerosol layers originates from wild and controlled fires. Although these fire plumes occur at ground level, they are lifted higher in the atmosphere due to the increased heat and may be

transported above Elandsfontein. Domestic biomass burning in informal settlements for cooking and heating can also contribute, but these emissions are exclusively emitted at ground level. It is therefore unlikely that such emission close to Elandsfontein will have a significant impact to free tropospheric aerosol load measured. However, household emissions are common across the entire southern Africa, which implies that regional transport of such emission further away from Elandsfontein may results in a contribution to the free tropospheric load measured over Elandsfontein. The absorbing smoke aerosols, originating from all the afore-mentioned combustion sources, can explain the large lidar ratio values observed. During this period the Ångström exponents appear to have large variation, with smaller values observed for lower aerosol layers. Ångström exponents appear to be lower from May to September. This can be attributed to the lower precipitation (dry season). Therefore larger particles stay longer in the atmosphere at lower layers, since they are not washed out. Also, particles can grow through accumulation during the dry season resulting to lower Ångström exponents.

The seasonal frequency distribution plots for the lidar ratio at 355 nm and the Ångström exponent related to extinction between 355 and 532 nm are presented in Figure 10 and 11, respectively. We present the frequency distribution plot only for 355 nm because observation of the lidar ratio at 532 nm was more often limited due to detector problems. Additional information on the intensive optical properties for both wavelengths is given in Table 3. The value in the table represent the mean value and one standard deviation. The numbers in brackets are the median value, while the number in parenthesis are the number of free tropospheric aerosol layers averages in each season (summer, autumn, winter, spring) or period (wet, dry, biomass). An average lidar ratio of 67 ± 25 sr at 355 nm and a mean extinction-related Ångström

458 exponent of 1.9 ± 0.8 between 355 and 532 nm are measured during the entire
459 sampling period in South Africa.
460 Lower mean values of lidar ratio and larger Ångström exponents have been observed
461 during summer. One possible explanation is the removal of larger aerosols through
462 wet-scavenging during these wetter months. Most of the free-tropospheric aerosol
463 layers observed during this period were associated with an easterly air mass flow. The
464 major industrial pollution sources are located primarily either to the north, west or
465 southwest of the lidar at Elandsfontein (Laakso et al., 2012). Therefore, the easterly
466 flow that prevails during summer results in a less polluted free troposphere, compared
467 to other seasons. Aerosols measured during this period could also include maritime
468 aerosols with air masses moving from the Indian Ocean.
469 However, we should note that during summer the Ångström exponent related to
470 backscatter between 355 and 532 nm is 1.5 ± 0.6 much smaller than Ångström
471 exponent related to extinction in the same wavelength range which is 2.4 ± 0.9. The
472 number of averaged layers to derive the Ångström exponent related to extinction
473 during summer is 17, while for Ångström exponent related to backscatter is 52. For
474 this reason we select only those layers, for which all five intensive optical properties
475 were retrieved (15). Significant spectral dependence of the lidar ratio values during
476 summer is observed which results in quite different values of Ångström exponent
477 related to backscatter and Ångström exponent related to extinction values. The mean
478 ratio of lidar ratio between 355 and 532 nm is 0.64 ± 0.23 during summer, while it is
479 larger and close to one for the rest of the seasons (autumn: 0.96 ± 0.3; winter: 0.82 ±
480 0.21, spring: 0.94 ± 0.29). The results during summer must be considered to be only
481 indicative since the number of aerosol layers averaged during summer is only 15 (less

Comment [HL1]: same amount of decimals

than the half compared to other seasons). More data should be collected and analyzed for a more accurate conclusion.

The frequency distribution plots of lidar ratio for autumn and winter are quite similar. However, 16% of elevated aerosols during autumn are associated with lidar ratios lower than 40 sr, while 12 % of lidar ratios were lower than 40 sr during winter. Seven-day backward trajectory analysis clearly indicated that these aerosol plumes (with lidar ratio lower than 40 sr), passed above the ocean in low heights. Wild fires in late July and August (see Figure 7(b)) are the mainly sources of absorbing smoke aerosols that result in aerosol layer plumes with high lidar ratios during these months. The intensive biomass burning activity in South Africa during spring is clearly reflected on the frequency distribution of the lidar ratio at 355 nm indicated by larger lidar ratio values, with a peak between 80 and 100 sr.

The frequency distribution plots of the extinction related Ångström exponent between 355 nm and 532 nm in Figure 11 reveal relatively evenly spread values during summer and autumn with no specific peak. This can most likely be attributed to atmospheric mixing processes. Ångström exponent distribution plot during winter and spring are similar, with a narrow distribution around 1.75.

~~Several statistics of lidar ratio and Ångström exponent are available for comparison. Mean lidar ratios at 355 nm vary from 21 to 67 sr, whereas 26 to 87 sr is found for the lidar ratio at 532 nm for aged Siberian forest fire smoke (Müller et al. 2005). Anderson et al. (2003) found a mean lidar ratio of 45 ± 10 sr at 532 nm during the ACE-Asia campaign in the spring of 2000 for east Asian haze over the Pacific Ocean close to China. Murayama et al. (2003) analyzed ACE Asia lidar and aircraft measurements over Japan. Mean lidar ratios in the polluted lower troposphere were 35-45 sr, and Ångström exponents were 1.5-2 in the wavelength range from 450 to~~

~~700 nm. Bösenberg et al. (2003) report an average lidar ratio of 55 sr at 351 nm for height range 2000 to 3000 m over Hamburg, Germany. Giannakaki et al. (2010) analyzed 7 years of EARLINET observations (2001–2007). Lidar ratio at 355 nm of the order of 70 sr was found for biomass burning aerosols. Amiridis et al. (2009) found that backscatter related Ångström exponent for biomass burning aerosols over Southeastern Europe ranges between 0.5 and 2.4 indicating a variety of particle sizes. Giannakaki et al. (2010) found that Ångström exponent ranges from 1 to 3 both for biomass burning aerosols and European continental polluted aerosols, indicating the same size of aerosols for these types of aerosols. An Ångström exponent of 1.35 was measured for Siberian forest fire smoke at Tokyo (Murayama et al., 2004). Mean particle Ångström exponent between 355 and 532 nm varied from 0 to 1.3 for aged biomass burning aerosols observed over central Germany (Müller et al., 2005). A decrease of the Ångström exponent (450 – 550 nm wavelength), which is equivalent to an increase of particle size, was observed for fires in tropical forest and cerrado during SCAR B campaign (Reid et al., 1998). In situ observations showed that Ångström exponents (355-532 nm wavelength) were on the order of 2.2 ± 0.2 for fresh smoke and 1.2 ± 0.2 for aged smoke. Moreover, different biomass fuel and burning processes certainly generate particles of different initial size, which in the end may lead to different growth mechanisms.~~

~~In this study large variability is observed both for lidar ratio and Ångström exponent of free tropospheric aerosol layers throughout the year. During summer, autumn and winter lidar ratio and Ångström exponents are within the range of previous observation for urban/industrial aerosols (Müller et al., 2007; Giannakaki et al., 2010; Bösenberg et al., 2003). During spring the lidar ratio of elevated layers is high, on average 89 sr, which is comparable to biomass burning smoke (Giannakaki et al.,~~

~~2010; Amiridis et al., 2009). Mean Ångström exponent during spring found to be 1.8 ± 0.5, indicating relatively small and fresh biomass burning particles.~~

3.3 Comparison with prior studies

This study is the first long-term lidar study of intensive and extensive optical aerosol properties in South Africa. Large variability is observed both for lidar ratio and Ångström exponent of free tropospheric aerosol layers throughout the year. Several statistics of lidar ratio and Ångström exponent are available for comparison and discussion.

3.3.1 Lidar ratio

During spring the lidar ratio of elevated layers is high, on average 89 sr. The large lidar ratio values during this period is attributed to biomass burning aerosol layers. Mean lidar ratios at 355 nm vary from 21 to 67 sr, whereas 26 to 87 sr is found for the lidar ratio at 532 nm for aged Siberian forest fire smoke (Müller et al. 2005). Giannakaki et al. (2010) analyzed 7 years of EARLINET observations (2001 -2007) and found lidar ratio at 355 nm of the order of 70 sr for biomass burning aerosols .

During summer and autumn lidar ratio values at 355 nm are 57 ± 20 and 59 ± 22 sr, respectively. These values are within the range of previous observation for urban/industrial aerosols (Müller et al., 2007; Giannakaki et al., 2010; Bösenberg et al., 2003). Anderson et al. (2003) found a mean lidar ratio of 45 ± 10 sr at 532 nm during the ACE-Asia campaign in the spring of 2000 for east Asian haze over the Pacific Ocean close to China. Murayama et al. (2003) analyzed ACE-Asia lidar and aircraft measurements over Japan and found mean lidar ratios of 35-45 sr in the polluted lower troposphere. Bösenberg et al. (2003) report an average lidar ratio of 55 sr at 351 nm for height range 2000 to 3000 m over Hamburg, Germany.

During winter mean lidar ratio at 355 nm was found equal to 65 ± 23 sr, larger than the values for summer and autumn. These aerosol layers are attributed mainly to

Formatted: Heading 1, Left, Line spacing: single

Formatted: Line spacing: Double

Formatted: Heading 1, Left

Formatted: Line spacing: Double

Formatted: Font: 12 pt

urban/industrial aerosols during June and July while during August the aerosol layers are possible a mixture of urban/industrial aerosols with biomass burning aerosols.

3.3.2 Ångström exponent

In this study we report mean Ånsgtröm exponent of 2.4 ± 0.9, 1.8 ± 0.9, 1.8 ± 0.6 and 1.8 ± 0.6 for summer, autumn, winter and spring respectively. As discussed in section 3.2 the results for Ångström exponent during summer must be considered to be only indicative since the number of aerosol layers averaged during summer is limited. For the rest of the seasons the values of Ångström exponent agree very well with former studies.

Murayama et al. (2003) have found Ångström exponents of 1.5-2 in the wavelength range from 450 to 428 700 nm on the polluted lower troposphere over Japan. Giannakaki et al. (2010) have found large variation of Ångström exponent for European continental anthropogenic aerosols which was attributed to different aerosol sources.

For biomass burning aerosols Amiridis et al. (2009) found that backscatter related Ångström exponent over Southeastern Europe ranges between 0.5 and 2.4 indicating a variety of particle sizes. An Ångström exponent of 1.35 was measured for Siberian forest fire smoke at Tokyo (Murayama et al., 2004). Mean particle Ångström exponent between 355 and 532 nm varied from 0 to 1.3 for aged biomass burning aerosols observed over central Germany (Müller et al., 2005). Giannakaki et al. (2010) found that Ångström exponent ranges from 1 to 3 both for biomass burning aerosols and European continental polluted aerosols, indicating the same size of aerosols for these types of aerosols.

4. Summary and conclusions

The seasonal patterns of the geometrical characteristics and optical properties of elevated aerosol layers at a continental site in South Africa are presented. The geometrical depth of the free tropospheric layers varies from a few hundred meters to

Formatted: Heading 1, Left, Line spacing: single

Formatted: Line spacing: Double

several kilometers. ~~Pollution events~~ The free-tropospheric aerosol layers are observed as single layer on 52% of the cases, while they are often characterized by two (32 %), three (13 %) or more particle layers (3%). Several aerosol sources may be responsible for a single free tropospheric pollution event. The classification of the aerosol layers in respect ~~relating~~ to the season of occurrence revealed rather stable geometrical aerosol layer depths for winter, summer and autumn with higher aerosol layer depths during spring. During winter nights layers are observed up to 3000 m. These aerosol layers are probably trapped between the inversion surface layer and an absolutely stable layer that is formed in 90% of days during winter (Cosijn and Tyson, 1996).

Except for the intensive biomass burning period from August to October, the lidar ratios and Ångström exponents are within the range of previous observations for urban/industrial aerosols (Müller et al., 2007; Giannakaki et al., 2010; Bösenberg et al., 2003). Considering that the Elandsfontein measurement station is located in the midst of large industrial plants 150 km east of the megacity of Johannesburg, this is reasonable. However, we observed large variability in both intensive and extensive aerosol properties of free tropospheric aerosol layers. From August to October, the lidar ratio of elevated layers is high, on average 89 sr, which is comparable to biomass burning smoke (Giannakaki et al., 2010; Amiridis et al., 2009). During this period also AOD is significantly increased, suggesting that similar to ground-based aerosol in the region (e.g. Vakkari et al., 2013) the seasonality of elevated aerosol layers is dominated by combustion sources. The mean free tropospheric contribution to the AOD of aerosol layers is 46% which can reach up to 96%. Mean Ångström exponent related to extinction was found to be 1.8 both for dry and biomass burning period indicating the same size of particles for both biomass burning and polluted aerosols.

ACKNOWLEDGMENTS

This work has been partly supported by the European Commission 6th Framework program under the EUCAARI project (contract no. 036833-2). Elina Giannakaki acknowledges the support of the Academy of Finland (project no. 270108). The authors acknowledge the staff of the North-West University for valuable assistance and routine maintenance of the lidar. We also acknowledge Eskom and Sasol for their logistical support for measurements at Elandsfontein.

REFERENCES

Althausen, D., Engelmann, R., Baars, H., Heese, B., Ansmann, A., Müller, D., and Komppula, M.: Portable Raman Lidar Polly^{XT} for Automated Profiling of Aerosol Backscatter, Extinction, and Depolarization, J. Atmos. Ocean. Technol., 26, 2366-2378, doi: 10.1175/2009jtecha1304.1, 2009.

Amiridis, V., Balis, D. S., Kazadzis, S., Bais, A., Giannakaki, E., Papayannis, A., and Zerefos, C.: Four-year aerosol observation with a Raman lidar at Thessaloniki, Greece, in the framework of the European Aerosol Research Lidar Network (EARLINET), J. Geophys. Res., 110, D21203, doi: 10.1029/2005JD006190, 2005.

Amiridis, V., Balis, D. S., Giannakaki, E., Stohl, A., Kazadzis, S., Koukouli, M. E., and Zanis, P.: Optical characteristics of biomass burning aerosols over Southeastern Europe determined from UV-Raman lidar measurements, Atmos. Chem. Phys., 9, 2431-2440, doi:10.5194/acp-9-2431-2009, 2009.

Anderson, T.L., Masonis, S. J., Covert, D. S., Ahlquist, N. C., Howell, S. G., Clarke, A. D., and McNaughton, C. S.: Variability o aerosol optical properties derived from in situ aircraft measurements during ACE-Asia, J. Geophys. Res., 108 (D23), 8647, doi: 10.1029/2002JD003247, 2003.

Andreae, M. O., Rosenfeld, D., Artaxo, P., Costa, A. A., Frank, G. P., Longo, K. M., and Silva-Dias, M. A. F., Smoking rain clouds over the Amazon, Science, 303, 1337-1342, doi: 10.1126/science.1092779, 2004.

Ångström, A.: The parameters of atmospheric turbidity, Tellus, 16, 64-75, doi: 10.1111/j.2153-3490.1964.tb00144.x, 1964.

Ansmann, A., Wandinger, U., Riebesell, M., Weitkamp, C., and Michaelis, W.: Independent measurement of extinction and backscatter profiles in cirrus clouds by using a combined Raman elastic-backscatter lidar, Appl. Optics, 31, 7113-7131, doi: 10.1364/AO.31.007113,1992.

Ansmann, A., Wagner, F., Müller, D., Althausen, D., Herber, A., von Hoyningen-Huene, W., and Wandinger, U.: European pollution outbreaks during ACE 2: Optical

particle properties inferred from multiwavelength lidar and star-Sun photometry, J. Geophys. Res., 107, doi: 10.1029/2001jd001109, 2002.

Baars, H., Ansmann, A., Althausen, D., Engelmann, R., Heese, B., Müller, D., Artaxo, P., Paixao, M., Pauliquevis, T., and Souza, R.: Aerosol profiling with lidar in Amazon Basin during the wet and dry season, J. Geophys. Res., 117, D21201, doi: 10.1029/2012JD018338, 2012.

Balis, D. S., Amiridis, V., Nickovic, S., Papayannis, A., and Zerefos, C.: Optical properties of Saharan dust layers as detected by a Raman lidar at Thessaloniki, Greece, Geophys. Res. Lett., 31, L13104, doi: 10.1029/2004gl019881, 2004.

Brooks, I. M.: Finding boundary layer top: Application of a wavelet covariance transform to lidar backscatter profiles, Journal of Atmos. and Ocea. Technol., 20, 1092-1105, doi: 10.1175/1520-0426(2003)020<1092:FBLTAO>2.0.CO;2, 2003.

Bryant R. G., Bigg, G. R., Mahowald, N. M., Eckardt F. D., and Ross, S. G. : Dust emission response to climate in southern Africa, J. Geophys. Res., 112, D09207, doi: 10.1029/2005JD007025, 2007.

Bösenberg et al. : EARLINET: A European Aerosol Research Lidar Network to establish an Aerosol Climatology, Technical report No. 348, 6-31, 2003.

Campbell, J. R., Welton, E. J., Spinhirne, J. D., Ji, Q., Tsay, S. C., Piketh, S. J., Barenbrug, M., and Holben, B. N.: Micropulse lidar observations of tropospheric aerosols over northeastern South Africa during the ARREX and SAFARI 2000 dry season experiments, J. Geophys. Res., 108, D13, 8497, doi: 10.1029/2002jd002563, 2003.

Cosijn, C. and Tyson, P. D.: Stable discontinuities in the atmosphere over South Africa, S. Afr. J. Sci., 92, 381–386, 1996.

Draxler, R. R. and Hess, G. D.: Description of the HYSPLIT 4 modeling system, NOAA Tech Memo, ERL ARL-224, 24, NOAA, Silver Spring, Md., 1997.

Draxler, R. R. and Hess, G. D.: An overview of the HYSPLIT 4 modelling system for trajectories, dispersion and deposition, Aust. Meteorol. Mag., 47, 295–308, 1998.

Field Code Changed

672 Eck, T. F., Holben, B. N., Ward, D. E., Mukelabai, M. M., Dubovik, O., Smirnov, A.,
673 Schafer, J. S., Hsu, N. C., Piketh, S. J., Queface, A., Le Roux, J., Swap, R. J., and
674 Slutsker, I.: Variability of biomass burning aerosol optical characteristics in southern
675 Africa during the SAFARI 2000 dry season campaign and a comparison of single
676 scattering albedo estimates from radiometric measurements, J. Geophys. Res., 108,
677 D13, 8477, doi: 10.1029/2002jd002321, 2003.

678 Engelmann R., Althausen, D., Heese, B., Baars, H., Komppula, M. : Recent upgrades
679 of the multiwavelength polarization raman lidar polly^{XT}, 22nd International Laser and
680 Radar Conference, Porto Heli, Greece, S1P-25, 2012.

681 Flamant, C., Pelon, J., Flamant, P. H., and Durand, P.: Lidar determination of the
682 entrainment zone thickness at the top of the unstable marine atmospheric boundary
683 layer, Bound.-Lay. Meteorol., 83, 247-284, doi: 10.1023/a:1000258318944, 1997.

684 Formenti, P., Winkler, H., Fourie, P., Piketh, S., Makgopa, B., Helas, G., and
685 Andreae, M. O.: Aerosol optical depth over a remote semi-arid region of South Africa
686 from spectral measurements of the daytime solar extinction and the nighttime stellar
687 extinction, Atmos. Res., 62, 11-32, doi: 10.1016/s0169-8095(02)00021-2, 2002.

688 Formenti, P., Elbert, W., Maenhaut, W., Haywood, J., Osborne, S., and Andreae, M.
689 O.: Inorganic and carbonaceous aerosols during the Southern African Regional
690 Science Initiative (SAFARI 2000) experiment: Chemical characteristics, physical
691 properties, and emission data for smoke from African biomass burning, J. Geophys.
692 Res., 108, D13, 16, doi: 10.1029/2002jd002408, 2003.

693 Freiman, M. T., and Piketh, S. J.: Air transport into and out of the industrial Highveld
694 region of South Africa, J. Appl. Meteorol., 42, doi: 10.1175/1520-
695 0450(2003)042<0994:ATIAOO>2.0.CO;2, 994-1002, 2003.

696 Giannakaki, E., Balis, D. S., Amiridis, V., and Zerefos, C.: Optical properties of
697 different aerosol types: seven years of combined Raman-elastic backscatter lidar
698 measurements in Thessaloniki, Greece, Atmos. Meas. Tech., 3, 569-578, doi:
699 10.5194/amt-3-569-2010, 2010.

Field Code Changed

Giglio, L., Randerson, J. T., van der Werf, G.R., Kasibhatla, P. S., Collatz, G. J., Morton, D. C., and DeFries, R. S.: Assessing variability and long-term trends in burned area by merging multiple satellite fire products, Biogeosciences, 7, 1171-1186, doi: 10.5194/bg-7-1171-2010, 2010.

Groß, S., Esselborn, M., Weinzierl, B., Wirth, M., Fix, A., and Petzold, A.: Aerosol classification by airborne high spectral resolution lidar observations, Atmos. Chem. Phys., 13, 2487-2505, doi: 10.5194/acp-13-2487-2013, 2013.

Hantson S., Padilla, M., Corti, D., and Chuvieco, E. : Strengths and weaknesses of MODIS hotspots to characterize global fire occurrence, Remote Sens of Environ, 131, 152-159, doi:10.1016/j.rse. 2012.12.004, 2013.

Hänel, A., Baars, H., Althausen, D., Ansmann, A., Engelmann, R., and Sun, Y. J.: One-year aerosol profiling with EUCAARI Raman lidar at Shangdianzi GAW station: Beijing plume and seasonal variation, J. Geophys. Res., 117, D13201, doi :10.1029/2012JD017577, 2012.

Hirsikko A., O´Connor, E. J., Komppula, M., Korhonen, K., Pfüller, A., Giannakaki, E., Wood, C. R., Bauer-Pfundstein, M., Poikonen, A., Karppinen, T., Lonka, H., Kurri, M., Heinonen, J., Moisseev, D., Asmi, E., Aaltonen, V., Nordbo, A., Rodriguez, E., Lihavainen, H., Laaksonen, A., Lehtinen, K.E.J., Laurila, T., Petäjä, T., Kulmala, M., and Viisanen, Y. : Observing wind, aerosol particles, cloud and precipitation: Finland's new ground-based remote-sensing network, Atmos. Meas. Tech., 7, 1351-1375, doi: 10.5194/amt-7-1351-2014 2014.

Holben, B. N., Eck, T. F., Slutsker, I., Tanre, D., Buis, J. P., Setzer, A., Vermote, E., Reagan, J. A., Kaufman, Y. J., Nakajima, T., Lavenu, F., Jankowiak, I., and Smirnov, A.: AERONET - A federated instrument network and data archive for aerosol characterization, Remote Sens. Environ., 66, 1-16, doi: 10.1016/s0034-4257(98)00031-5, 1998.

Hsu, N. C., Herman, J. R., and Weaver, C.: Determination of radiative forcing of Saharan dust using combined TOMS and ERBE data, J. Geophys. Res., 105, D16, 20649-20661, doi: 10.1029/2000jd900150, 2000.

729 Ichoku, C., Remer, L. A., Kaufman, Y. J., Levy, R., Chu, D. A., Tanre, D., and
730 Holben, B. N.: MODIS observation of aerosols and estimation of aerosol radiative
731 forcing over southern Africa during SAFARI 2000, J. Geophys. Res., 108, 13, doi:
732 10.1029/2002jd002366, 2003.

733 IPCC: The Physical Science Basis, Contribution of Working Group I to the Fifth
734 Assessment Report of the Intergovernmental Panel on Climate Change, edited by :
735 Stocker, T. F., Qin, D., Plattner, G.-K, Tignor, M., Allen, S. K., Boschung, J., Nauels,
736 A., Xia, Y., Bex, V., and Midgley, P. M., Cambridge University Press, Cambridge,
737 United Kingdom and New York, NY, USA, 2013.

738 Ito, A., Ito, A., and Akimoto, H. : Seasonal and interannual variations in CO and BC
739 emissions from open biomass burning in Southern Africa during 1998-2005, Global
740 Biogeochem. Cy., 21, GB2011, doi: 10.1029/2006GB002848, 2007.

741 Klett, 1981: Stable analytical inversion solution for processing lidar returns, Appl.
742 Optics, 20, 211-220, doi: 10.1364/AO.20.000211, 1981.

743 Komppula, M., Mielonen, T., Arola, A., Korhonen, K., Lihavainen, H., Hyvärinen, A.
744 P., Baars, H., Engelmann, R., Althausen, D., Ansmann, A., Müller, D., Panwar, T. S.,
745 Hooda, R. K., Sharma, V. P., Kerminen, V. M., Lehtinen, K. E. J., and Viisanen, Y.:
746 Technical Note: One year of Raman-lidar measurements in Gual Pahari EUCAARI
747 site close to New Delhi in India - Seasonal characteristics of the aerosol vertical
748 structure, Atmos. Chem. Phys., 12, 4513-4524, doi: 10.5194/acp-12-4513-2012, 2012.

749 Koren, I., Kaufman, Y. J., Remer, L. A., and Martins, J. V., Measurement of the effect
750 of Amazon smoke on inhibition of cloud formation, Science, 303, 1342-1345, doi:
751 10.1126/science.1089424, 2004.

752 Koren, I., Martins, J. V., Remer, L. A., and Afargan H.: Smoke invigoration versus
753 inhibition of clouds over the Amazon, Science, 321, 946-949, doi:
754 10.1126/science.1159185, 2008.

755 Korhonen, K., Giannakaki, E., Mielonen, T., Pfüller, A., Laakso, L., Vakkari, V.,
756 Baars, H., Engelmann, R., Beukes, J. P., Van Zyl, P. G., Ramandh, A., Ntsangwane,
757 L., Josipovic, M., Tiitta, P., Fourie, G., Ngwana, I., Chiloane K., and Komppula, M. :

758 Atmospheric boundary layer top height in South Africa: measurements with lidar and
759 radiosonde compared to three atmospheric models, Atmos. Chem. Phys., 14, 4263-
760 4278, doi: 10.5194/acp-14-4263-2014, 2014.

761 Kulmala, M., et al., General overview: European Integrated project on Aerosol Cloud
762 Climate and Air Quality interactions (EUCAARI) – integrating aerosol research from
763 nano to global scales, Atmos. Chem. Phys., 11, 13061-13143, doi: 10.5194/acp-11-
764 13061-2011, 2011.

765 Laakso, L., Vakkari, V., Virkkula, A., Laakso, H., Backman, J., Kulmala, M., Beukes,
766 J. P., van Zyl, P. G., Tiitta, P., Josipovic, M., Pienaar, J. J., Chiloane, K., Gilardoni,
767 S., Vignati, E., Wiedensohler, A., Tuch, T., Birmili, W., Piketh, S., Collett, K., Fourie,
768 G. D., Komppula, M., Lihavainen, H., de Leeuw, G., and Kerminen, V. M.: South
769 African EUCAARI measurements: seasonal variation of trace gases and aerosol
770 optical properties, Atmos. Chem. Phys., 12, 1847-1864, doi: 10.5194/acp-12-1847-
771 2012, 2012.

772 Lourens, A. S. M., Butler, T. M., Beukes, J. P., van Zyl, P. G., Beirle, S., Wagner, T.
773 K., Heue, K. P., Pienaar, J. J., Fourie, G. D., and Lawrence, M. G.: Re-evaluating the
774 NO2 hotspot over the South African Highveld, S. Afr. J. Sci., 108, doi: 54-59,
775 10.4102/sajs.v108i11/12.1146, 2012.

776 Marufu, L., Dentener, F., Lelieveld, J., Andreae, M. O., and Helas, G.:
777 Photochemistry of the African troposphere: Influence of biomass-burning emissions,
778 J. Geophys. Res., 105, 14513-14530, doi: 10.1029/1999jd901055, 2000.

779 Mattis, I., Muller, D., Ansmann, A., Wandinger, U., Preissler, J., Seifert, P., and
780 Tesche, M.: Ten years of multiwavelength Raman lidar observations of free-
781 tropospheric aerosol layers over central Europe: Geometrical properties and annual
782 cycle, J. Geophys. Res., 113, D20202, doi: 10.1029/2007jd009636, 2008.

783 Modis Fire Mapper website, http://earthdata.nasa.gov/data/nrt-data/firms/active-fire-
784 data, last accessed: 10.12.2014.

Field Code Changed

785 Mona, L., Amodeo, A., Pandolfi, M., and Pappalardo, G.: Saharan dust intrusions in
786 the Mediterranean area: Three years of Raman lidar measurements, J. Geophys. Res.,
787 111, D16203, doi: 10.1029/2005jd006569, 2006.

788 Müller, D., Ansmann, A., Wagner, F., Franke, K., and Althausen, D.: European
789 pollution outbreaks during ACE 2: Microphysical particle properties and single-
790 scattering albedo inferred from multiwavelength lidar observations, J. Geophys. Res.,
791 107, D15, 4248, doi: 10.1029/2001jd001110, 2002.

792 Müller, D., Franke, K., Ansmann, A., Althausen, D., and Wagner, F.: Indo-Asian
793 pollution during INDOEX: Microphysical particle properties and single-scattering
794 albedo inferred from multiwavelength lidar observations, J. Geophys. Res., 108, D19,
795 4600, doi: 10.1029/2003jd003538, 2003.

796 Müller, D., Mattis, I., Wandinger, U., Ansmann, A., Althausen, D., and Stohl, A.:
797 Raman lidar observations of aged Siberian and Canadian forest fire smoke in the free
798 troposphere over Germany in 2003: Microphysical particle characterization, J.
799 Geophys. Res., 110, D17201, doi: 10.1029/2004jd005756, 2005.

800 Müller, D., Ansmann, A., Mattis, I., Tesche, M., Wandinger, U., Althausen, D., and
801 Pisani, G.: Aerosol-type-dependent lidar ratios observed with Raman lidar, Journal of
802 Geophysical Research-Atmospheres, 112, D16202, doi: 10.1029/2006jd008292, 2007.

803 Murayama, T., Müller, D., Wada, K., Shimizu, A., Sekigushi, M., and Tsukamato, T.:
804 Characterization of Asian dust and Siberian smoke with multi-wavelength Raman
805 lidar over Tokyo, Japan in spring 2003, Geophys. Res. Lett., 31, L23103, doi:
806 10.1029/2004GL021105, 2004.

807 Murayama, T., Masonis, S. J., Redemann, J., Aderson, T. L., Schmid, B., Living J. M,
808 Russell, P. B., Huebert, B., Howell, S. G., McNaughton, C. S., Clarke, A., Abo, M.,
809 Shimizu, A., Sugimoto, N., Yabuki, M., Kuze, H., Fukagawa, S., Maxwell-Meier K.,
810 Weber, R. J., Orsini, D.A., Blomquist, B., Bandy, A., and Thornton, D.: An
811 intercomparison of lidar-derived aerosol optical properties with airborne
812 measurements near Toko during ACE-Asia, J. Geophys. Res., 108, D23, 8651, doi:
813 10.1029/2002JD003259, 2003.

814 Papayannis, A., Amiridis, V., Mona, L., Tsaknakis, G., Balis, D., Bosenberg, J.,
815 Chaikovski, A., De Tomasi, F., Grigorov, I., Mattis, I., Mitev, V., Muller, D.,
816 Nickovic, S., Perez, C., Pietruczuk, A., Pisani, G., Ravetta, F., Rizi, V., Sicard, M.,
817 Trickl, T., Wiegner, M., Gerding, M., Mamouri, R. E., D'Amico, G., and Pappalardo,
818 G.: Systematic lidar observations of Saharan dust over Europe in the frame of
819 EARLINET (2000-2002), J. Geophys. Res., 113, D10204, doi:
820 10.1029/2007jd009028, 2008.

821 Pappalardo G., Amodeo, A., Apituley, A., Comeron, A., Freudenthaler, V., Linné, H.,
822 Ansmann, A., Bösenberg, J., D'Amico, G., Mattis, I., Mona, L., Wandinger, U.,
823 Amiridis, V., Alados-Arboledas, L., Nicolae, D. and Wiegner, M. : EARLINET :
824 towards an advanced sustainable European aerosol lidar network, Atmos. Meas.
825 Tech., 7, 2389-2409, doi: 10.5194/amt-7-2389-2014, 2014.

826 Piketh, S. J., Tyson, P. D., and Steffen, W.: Aeolian transport from southern Africa
827 and iron fertilization of marine biota in the South Indian Ocean, S. Afr. J. Sci., 96,
828 244-246, 2000.

829 Piketh, S. J., Swap, R. J., Maenhaut, W., Annegarn, H. J., and Formenti, P.: Chemical
830 evidence of long-range atmospheric transport over southern Africa, J. Geophys. Res.,
831 107, D24, 4817, doi: 10.1029/2002jd002056, 2002.

832 Prospero, J. M., Ginoux, P., Torres, O., Nicholson, S. E., Gill, T., Environmental
833 characterization of global sources of atmospheric soil dust identified with the Nimbus
834 7 Total Ozone Mapping Spectrometer (TOMS) absorbing aerosol product, Rev.
835 Geophys, 40, 1002, doi: 10.1029/2000RG000095, 2002.

836 Queface, A. J., Piketh, S. J., Eck, T. F., Tsay, S. C., and Mavume, A. F.: Climatology
837 of aerosol optical properties in Southern Africa, Atmos. Environ., 45, 2910-2921, doi:
838 10.1016/j.atmosenv.2011.01.056, 2011.

839 Ramanathan, V., Crutzen, P. J., Kiehl, J. T., Rosenfeld, D.: Aerosols, climate, and the
840 hydrological cycle, Science, 294, 2119-2124, doi :10.1126/science.1064034, 2001.

841 Reid, J.S., Koppmann, R., Eck, T.F, and Eleuterio, D. P., A review of biomass
842 burning emissions, part II. Intensive physical properties of biomass burning particles,
843 Atmos. Chem. Phys., 5, 799-825, doi: 10.5194/acp-5-799-2005, 2005.

844 Robles-Gonzalez, C., and de Leeuw, G., Aerosol properties over the SAFARI-2000
845 area retrieved from ATSR-2, J. Geophys. Res., 113, D05206, doi:
846 10.1029/2007JD008636, 2008.

847 Rosenfeld, D., Lohmann, U., Raga, G. B., O'Dowd, C.D., Kulmala, M., Fuzzi, S.,
848 Reissell, A., and Andreae, M. O., Flood or drought : How do aerosols affect
849 precipitation, Science, 321, 1309-1313, doi: 10.1126/science.1160606, 2008.

850 Ross, K. E., Piketh, S. J., Bruintjes, R. T., Burger, R. P., Swap, R. J., and Annegarn,
851 H. J.: Spatial and seasonal variations in CCN distribution and the aerosol-CCN
852 relationship over southern Africa, J. Geophys. Res., 108, D13, 8481, doi:
853 10.1029/2002JD002384, 2003.

854 Roy, D. P., Boschetti, L., Justice, C. O. and Ju, J.: The collection 5 MODIS burned
855 area product – Global evaluation by comparison with the MODIS active fire product,
856 Remote Sens. Environ., 112, 3960-3707, doi: 10.1016/j.rse.2008.05.013, 2008.

857 Swap R. J., Annegarn, H. J., Suttles, J. T., King, M. D., Platnick, S., Privette, J. L.,
858 Scholes, R. J., Africa burning : A thematic analysis of the Southern African Regional
859 Science Initiative (SAFARI 2000), J. Geophys. Res., 108, D13, 8465, doi:
860 10.1029/2003JD003747, 2003.

861 Tesfaye, M., Sivakumar, V., Botai, J., and Tsidu, G. M.: Aerosol climatology over
862 South Africa based on 10 years of Multiangle Imaging Spectroradiometer (MISR)
863 data, J. Geophys. Res., 116, D20216, doi: 10.1029/2011jd016023, 2011.

864 Tiitta, P., Vakkari, V., Croteau, P., Beukes, J. P., van Zyl, P. G., Josipovic, M.,
865 Venter, A. D., Jaars, K., Pienaar, J. J., Ng, N. L., Canagaratna, M. R., Jayne, J. T.,
866 Kerminen, V.-M., Kokkola, H., Kulmala, M., Laaksonen, A., Worsnop, D. R., and
867 Laakso, L.: Chemical composition, main sources and temporal variability of PM1
868 aerosols in southern African grassland, Atmos. Chem. Phys., 14, 1909–1927, doi:
869 10.5194/acp-14-1909-2014, 2014.

Tummon, F., Solmon, F., Liousse, C., and Tadross, M. : Simulation of the direct and semidirect aerosol effects on the southern Africa regional climate during the biomass burning season, J. Geophys. Res., 115, D19206, doi: 10.1029/2009JD013738, 2010.

Tyson, P. D. and Preston-Whyte, R. A.: The Weather and Climate of Southern Africa, Oxford University Press, Cape Town, 2004.

Vaisala, available at: http://www.campbellsci.com/wxt510.

Vakkari, V., Kerminen, V.-M., Beukes, J. P., Tiitta, P., van Zyl, P. G., Josipovic, M., Venter, A. D., Jaars, K., Worsnop, D. R., Kulmala, M., and Laakso, L.: Rapid changes in biomass burning aerosols by atmospheric oxidation. Geophys. Res. Lett., 41, 2644–2651, doi: 10.1002/2014GL059396, 2014.

Vakkari, V., Beukes, J. P., Laakso, H., Mabaso, D., Pienaar, J. J., Kulmala, M., and Laakso, L.: Long-term observations of aerosol size distributions in semi-clean and polluted savannah in South Africa, Atmos. Chem. Phys., 13, 1751-1770, doi:10.5194/acp-13-1751-2013, 2013.

Venter, A. D., Vakkari, V., Beukes, J. P., van Zyl, P. G., Laakso, H., Mabaso, D., Tiitta, P., Josipovic, M., Kulmala, M., Pienaar, J. J., and Laakso, L.: An air quality assessment in the industrialised western Bushveld Ignous Complex, South Africa, S. Afr. J. Sci., 108, 1059, doi: 10.4102/sajs.v108i9/10.1059, 2012.

Wagner, F., Müller, D. and Ansmann, A.: Comparison of the radiative impact of aerosols derived from vertically resolved (lidar) and vertically integrated (Sun photometer) measurements: Example of an Indian aerosol plume, J. Geophys. Res., 106, D19, 22861- 22870, doi: 10.1029/2001JD000320, 2001.

Wandinger, U., and Ansmann, A.: Experimental determination of the lidar overlap profile with Raman lidar, Appl. Opt., 41, 511-514, doi: 10.1364/AO.41.000511, 2002.

Winkler, H., P. Formenti, D. J. Esterhuyse, R. J. Swap, G. Helas, H. J. Annegarn, and M. O. Andreae, Evidence for large-scale transport of biomass burning aerosols from sunphotometry at a remote South African site: Atmos. Environ., 42, 5569-5578, doi: 10.1016/j.atmosenv.2008.03.031, 2008.

Field Code Changed

TABLES

Table 1. Geometrical characteristics and AOD at 355 and 532 nm of free tropospheric aerosols for summer, autumn, winter, spring, wet, dry and biomass burning period. The values represent the mean value and one standard deviation. The numbers in brackets are the median value. The numbers in parenthesis are the number of free tropospheric aerosol layers averaged.

Season or period	Center (m)	AOD 355 nm	AOD 532 nm
Summer (Dec. – Feb.)	2440 ± 1100 (67) [2470]	0.07 ± 0.11 (56) [0.03]	0.05 ± 0.04 (18) [0.04]
Autumn (Mar. – May)	1800 ± 720 (116) [1740]	0.05 ± 0.04 (99) [0.04]	0.03 ± 0.02 (39) [0.02]
Winter (Jun – Aug)	1880 ± 1100 (98) [1685]	0.06 ±0.06 (78) [0.04]	0.04 ± 0.04 (40) [0.03]
Spring (Sep. – Nov.)	2520 ± 970 (94) [2415]	0.18 ± 0.14 (69) [0.15]	0.09 ± 0.07 (66) [0.08]
Wet (Oct. – Mar.)	2430 ± 1000 (174) [2375]	0.10 ± 0.10 (140) [0.06]	0.07 ± 0.05 (69) [0.06]
Dry (Apr. – Sep.)	1850 ± 950 (201) [1715]	0.08 ± 0.12 (162) [0.04]	0.05 ± 0.06 (94) [0.04]
Biomass burning (Aug. – Oct.)	2670 ± 1100 (106) [2535]	0.18 ± 0.13 (77) [0.15]	0.09 ± 0.07 (70) [0.08]

Table 2. Extensive optical properties of free tropospheric aerosol layers for summer , autumn, winter , spring, wet period, dry period, and biomass burning period. The values represent the mean value and one standard deviation. The numbers in brackets are the median value. The numbers in parenthesis are the number of free tropospheric aerosol layers averaged.

Season or period	Bsc. coef. 355 nm ($Mm^{-1}sr^{-1}$)	Bsc. coef. 532 nm ($Mm^{-1}sr^{-1}$)	Bsc. coef. 1064 nm ($Mm^{-1}sr^{-1}$)	Ext. coef. 355 nm (Mm^{-1})	Ext. coef. 532 nm (Mm^{-1})
Summer	2.7 ± 6.0 (62) [1.3]	1.0 ± 1.0 (52) [0.6]	0.7 ± 2.0 (62) [0.2]	118 ± 142 (56) [67]	82 ± 69 (18) [47]
Autumn	1.6 ± 1.0 (109) [1.3]	1.0 ± 0.8 (54) [0.8]	0.4 ± 0.2 (111) [0.3]	97 ± 65 (99) [77]	63 ± 36 (39) [63]
Winter	1.8 ± 1.3 (80) [1.5]	1.2 ± 1.0 (44) [1.0]	0.5 ± 0.4 (81) [0.4]	115 ± 93 (78) [83]	80 ± 55 (40) [64]
Spring	2.7 ± 1.3 (71) [2.6]	1. 5 ± 0.8 (71) [1.3]	0.6 ± 0.4 (71) [0.6]	232 ± 95 (69) [229]	118 ± 51 (66) [113]
Wet	2.4 ± 3.7 (149) [1.8]	1.2 ± 0.9 (112) [1.0]	0.6 ± 1.3 (149) [0.4]	147 ± 118 (140) [125]	98 ± 52 (69) [91]
Dry	1.8 ± 1.3 (173) [1.5]	1.2 ± 1.0 (109) [1.0]	0.5 ± 0.4 (176) [0.4]	127 ± 102 (162) [93]	87 ± 58 (94) [73]
Biomass	2.6 ± 1.2 (79) [2.5]	1.5 ± 0.8 (74) [1.3]	0.7 ± 0.4 (79) [0.6]	225 ± 88 (77) [223]	117 ± 47 (70) [113]

Table 3. Intensive optical properties of free tropospheric aerosol layers for summer, autumn, winter, spring, wet period, dry period and biomass burning period. The values represent the mean value and one standard deviation. The numbers in brackets are the median value. The numbers in parenthesis are the number of free tropospheric aerosol layers averaged.

Season or period	Lidar ratio 355 nm (sr)	Lidar ratio 532 nm (sr)	Ångström exp. b_{355}/b_{532}	Ångström exp. b_{532}/b_{1064}	Ångström exp. $\alpha_{355}/\alpha_{532}$
Summer	57 ± 20 (56) [59]	39 ± 18 (21) [31]	1.5 ± 0.6 (52) [1.5]	1.7 ± 0.5 (62) [1.7]	2.4 ± 0.9 (17) [2.3]
Autumn	59 ± 22 (99) [54]	58 ± 26 (41) [53]	1.8 ± 0.7 (98) [1.8]	1.3 ± 0.6 (106) [1.2]	1.8 ± 0.9 (39) [1.9]
Winter	65 ± 23 (78) [64]	60 ± 23 (40) [60]	1.5 ± 0.7 (72) [1.3]	1.2 ± 0.5 (78) [1.1]	1.8 ± 0.6 (40) [1.8]
Spring	89 ± 21 (69) [86]	82 ± 25 (66) [81]	1.6 ± 0.6 (71) [1.4]	1.2 ± 0.3 (71) [1.2]	1.8 ± 0.6 (59) [1.8]
Wet	67 ± 26 (140) [66]	69 ± 32 (72) [64]	1.6 ± 0.6 (138) [1.5]	1.5 ± 0.5 (149) [1.4]	2.0 ± 0.8 (62) [2.0]
Dry	67 ± 24 (162) [64]	63 ± 24 (96) [61]	1.6 ± 0.7 (155) [1.6]	1.2 ± 0.5 (168) [1.1]	1.8 ± 0.7 (93) [1.8]
Biomass	89 ± 20 (77) [87]	83 ± 23 (70) [81]	1.5 ± 0.6 (79) [1.4]	1.2 ± 0.3 (79) [1.2]	1.8 ± 0.5 (64) [1.8]

FIGURE captions

Figure 1. (a) Percentage of night-time analyzed measurements, scheduled shutdown and unanalyzed measurements ("no measurements") due to weather conditions (rain or clouds); (b) the percentage of measurements in which free tropospheric aerosol layers were observed (green bars) and the total number of the observed layers (red stars) per month; (c) monthly accumulated precipitation at Elandsfontein.

Figure 2. The hourly planetary boundary layer (a) and the difference between the bottom of the first free tropospheric layer observed and the planetary boundary (b) observed between 30th January 2010 and 31st January 2011.

Figure 3. Geometrical boundaries of free tropospheric aerosol layers observed between 30th January 2010 and 31st January 2011.

Figure 4. Geometrical characteristics and optical properties of free tropospheric aerosol layers observed between 30th January 2010 and 31st January 2011. From top to bottom: the center height of the layers observed (a), the geometrical depth of the layers observed (b), aerosol optical depths at 355 (blue) and 532 (green) nm (c). The number of free tropospheric aerosol layers averaged is also presented in the top of each figure.

Figure 5. Columnar optical depth at ultraviolet (a) and visible (b) wavelengths. Open squares corresponds to cimel daily mean values while filled circles corresponds to hourly night-time lidar values.

Figure 6. Variation of AOD at 355 nm (a) of the boundary layer (blue squares) and the free troposphere (orange circles) and (b) the monthly free tropospheric contribution ~~of~~ to total AOD at 355 nm. In (b) the squares represent the mean value, the horizontal line the median, the boxes the 25 and 75 % percentiles, the whiskers the standard deviation and the stars the maximum and minimum values during the respective month.

Figure 7. (a) Monthly variation of wind speed: the squares represent the mean value, the horizontal line the median, the boxes the 25 and 75 % percentiles and the whiskers the one standard deviation. (b) Number of hotspots over the region lat (40^{o}S, 20^{o}S) and lon (20^{o}E, 40^{o}E) with medium (blue) and high (red) confidence level.

Figure 8. Frequency distribution of center height of free-tropospheric aerosol layers in South Africa between 30th January 2010 and 31st January 2011, for (a) summer, (b) autumn, (c) winter and (d) spring. Box and whisker plots are also presented for each of the seasons: filled square is the mean value, horizontal line is the median, boxes are the 25 and 75 % percentiles respectively, whiskers represent the one standard deviation and stars the minimum and maximum values.

Figure 9. Intensive layer properties of the free tropospheric aerosol layers observed between 30th January 2010 and 31st January 2011. From top to bottom: (a) Ångström exponent related to backscatter between 355 and 532 nm (grey), related to backscatter

between 532 and 1064 nm (orange) and related to extinction between 355 and 532 nm (black) and (b) Lidar ratio at 355 (blue) and 532 (green) nm.

Figure 10. Frequency distribution of lidar ratio at 355 nm of free tropospheric aerosol layers in South Africa between 30th January 2010 and 31st January 2011, for (a) summer, (b) autumn, (c) winter and (d) spring. Box and whisker plots are also presented for each of the seasons: filled square is the mean value, horizontal line is the median, boxes are the 25 and 75 % percentiles respectively, whiskers represent the one standard deviation and stars the minimum and maximum values.

Figure 11. Frequency distribution of extinction related Ångström exponent between 355 and 532 nm of free tropospheric aerosol layers in South Africa between 30th January 2010 and 31st January 2011, for (a) summer, (b) autumn, (c) winter and (d) spring. Box and whisker plots are also presented for each of the seasons: filled square is the mean value, horizontal line is the median, boxes are the 25 and 75 % percentiles respectively, whiskers represent the one standard deviation and stars the minimum and maximum values.

985 **Figure 1**

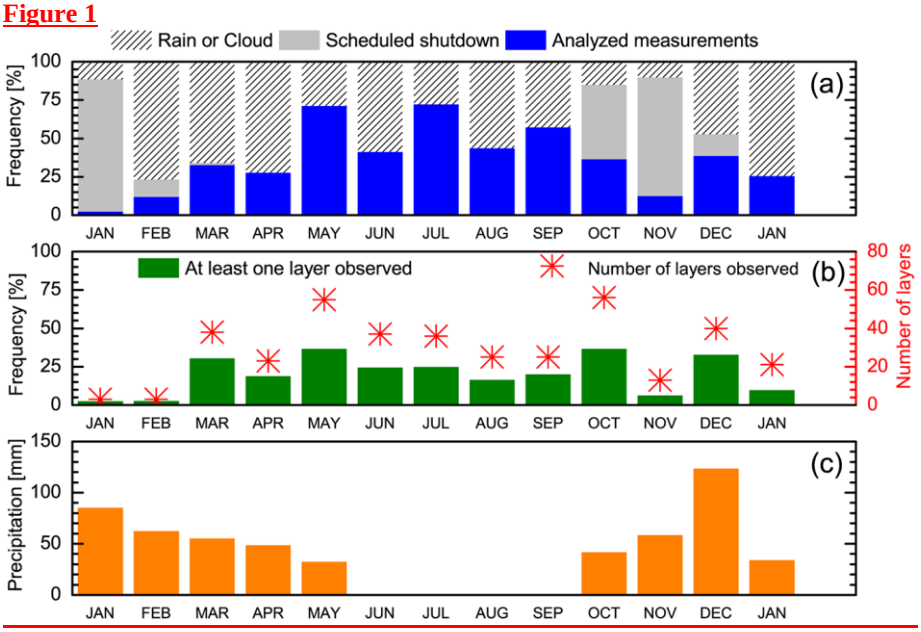

986
987

Figure 2

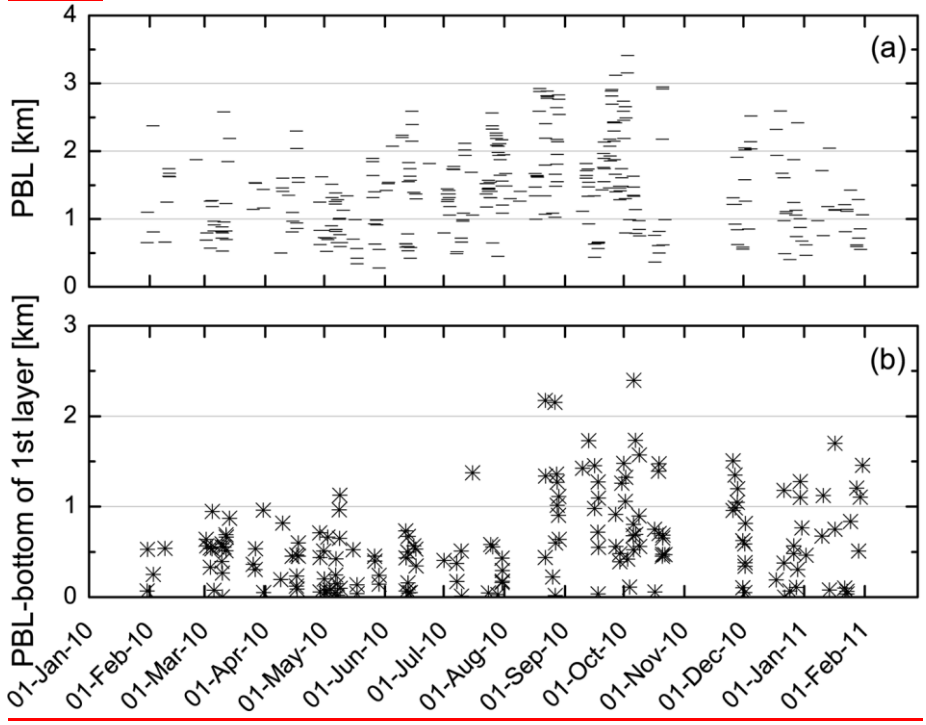
(a)
PBL [km]
0
1
2
3
4
(b)
PBL-bottom of 1st layer [km]
0
1
2
3
01-Jan-10
01-Feb-10
01-Mar-10
01-Apr-10
01-May-10
01-Jun-10
01-Jul-10
01-Aug-10
01-Sep-10
01-Oct-10
01-Nov-10
01-Dec-10
01-Jan-11
01-Feb-11

Figure 3

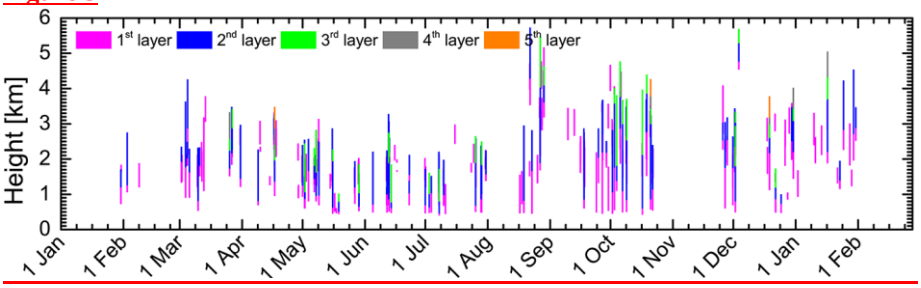
1st layer
2nd layer
3rd layer
4th layer
5th layer
Height [km]
0
1
2
3
4
5
6
1 Jan
1 Feb
1 Mar
1 Apr
1 May
1 Jun
1 Jul
1 Aug
1 Sep
1 Oct
1 Nov
1 Dec
1 Jan
1 Feb

Figure 4

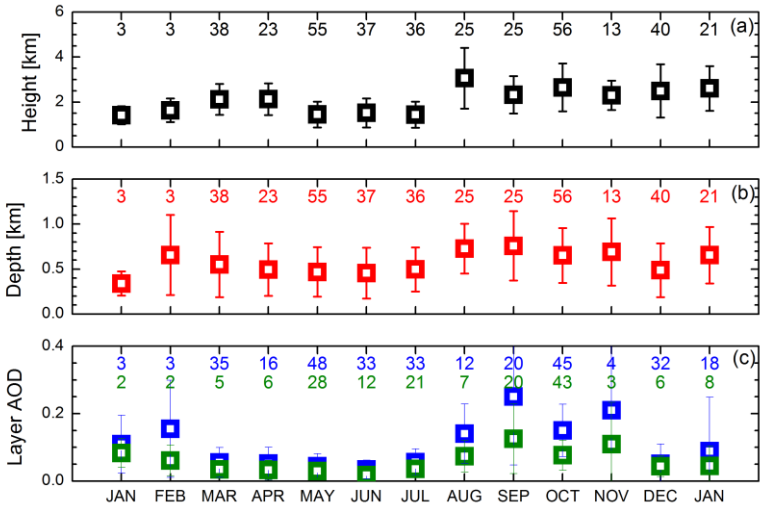
Height [km]
Depth [km]
Layer AOD
(a)
(b)
(c)
3 3 38 23 55 37 36 25 25 56 13 40 21
3 3 38 23 55 37 36 25 25 56 13 40 21
3 3 35 16 48 33 33 12 20 45 4 32 18
2 2 5 6 28 12 21 7 20 43 3 6 8
JAN FEB MAR APR MAY JUN JUL AUG SEP OCT NOV DEC JAN

998 **Figure 5**

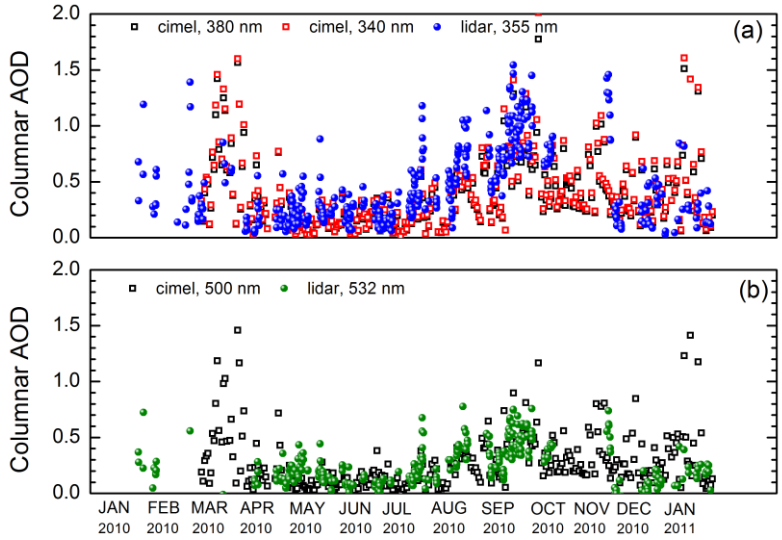

999
1000

Figure 6

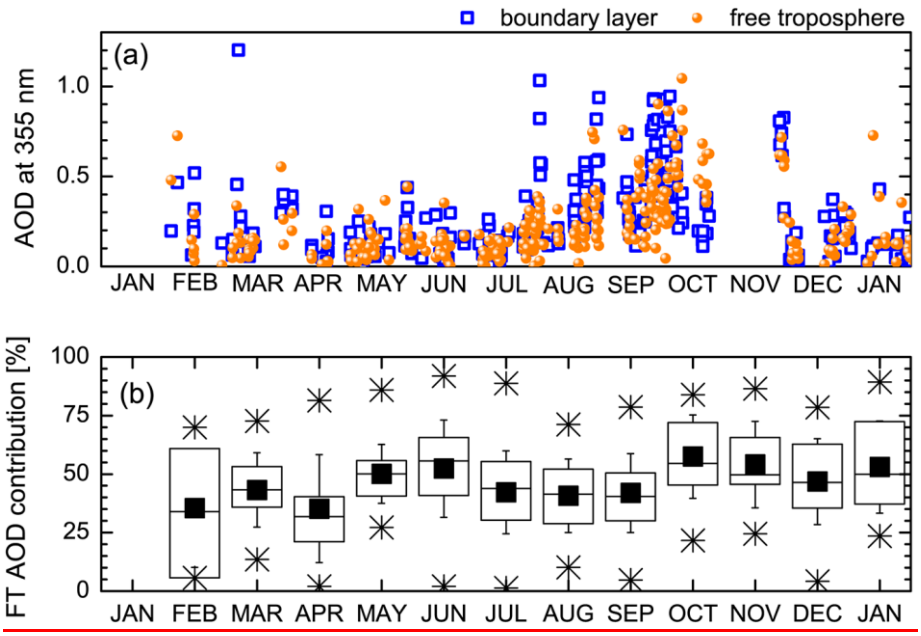
boundary layer
free troposphere
(a)
AOD at 355 nm
1.0
0.5
0.0
JAN FEB MAR APR MAY JUN JUL AUG SEP OCT NOV DEC JAN
(b)
FT AOD contribution [%]
100
75
50
25
0
JAN FEB MAR APR MAY JUN JUL AUG SEP OCT NOV DEC JAN

Figure 7

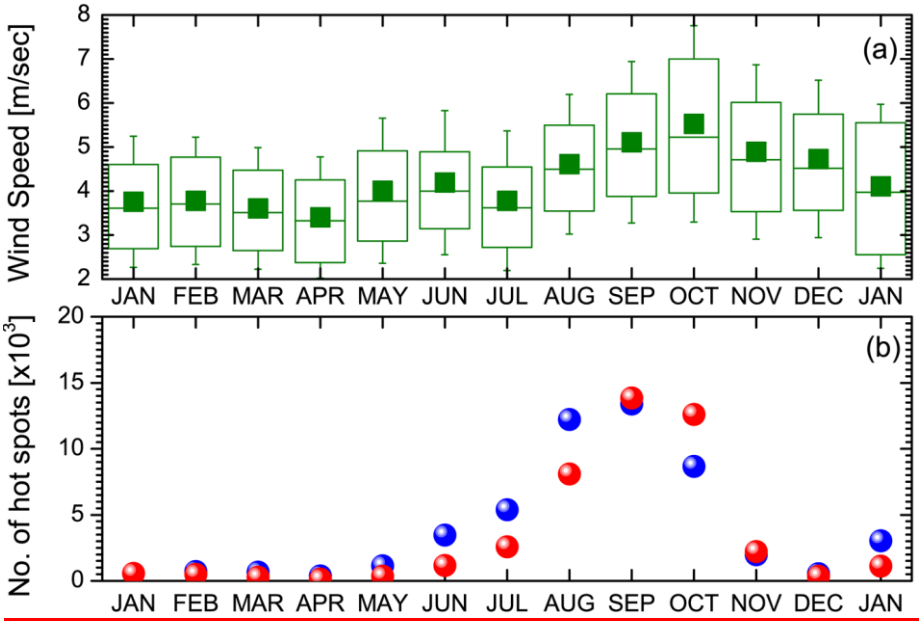
Wind Speed [m/sec]
(a)
JAN FEB MAR APR MAY JUN JUL AUG SEP OCT NOV DEC JAN
No. of hot spots [x10^3]
(b)
JAN FEB MAR APR MAY JUN JUL AUG SEP OCT NOV DEC JAN

Figure 8

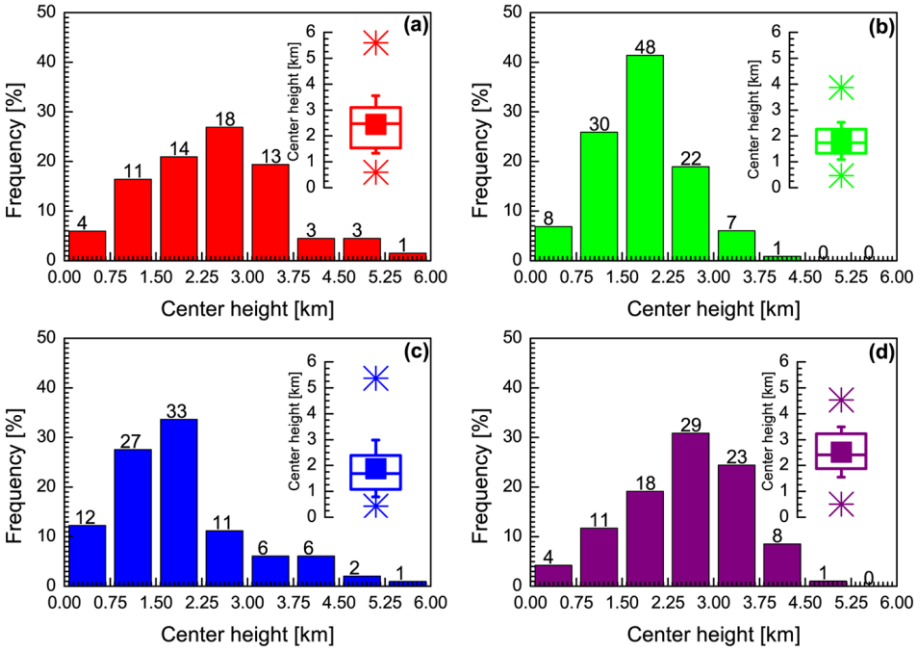
(a)
(b)
(c)
(d)
Frequency [%]
Center height [km]
Center height [km]
0.00 0.75 1.50 2.25 3.00 3.75 4.50 5.25 6.00
4 11 14 18 13 3 3 1
8 30 48 22 7 1 0 0
12 27 33 11 6 6 2 1
4 11 18 29 23 8 1 0

Figure 9

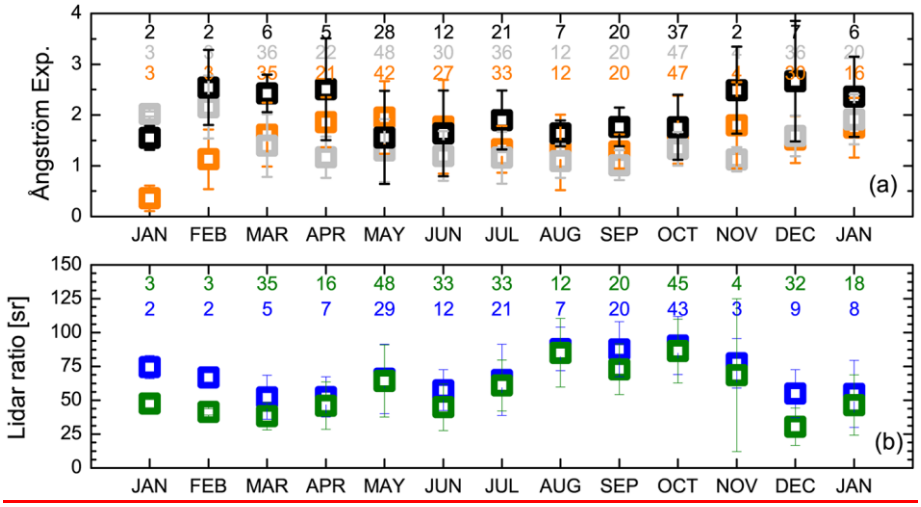
Ångström Exp.
(a)
JAN FEB MAR APR MAY JUN JUL AUG SEP OCT NOV DEC JAN
Lidar ratio [sr]
(b)
JAN FEB MAR APR MAY JUN JUL AUG SEP OCT NOV DEC JAN

Figure 10

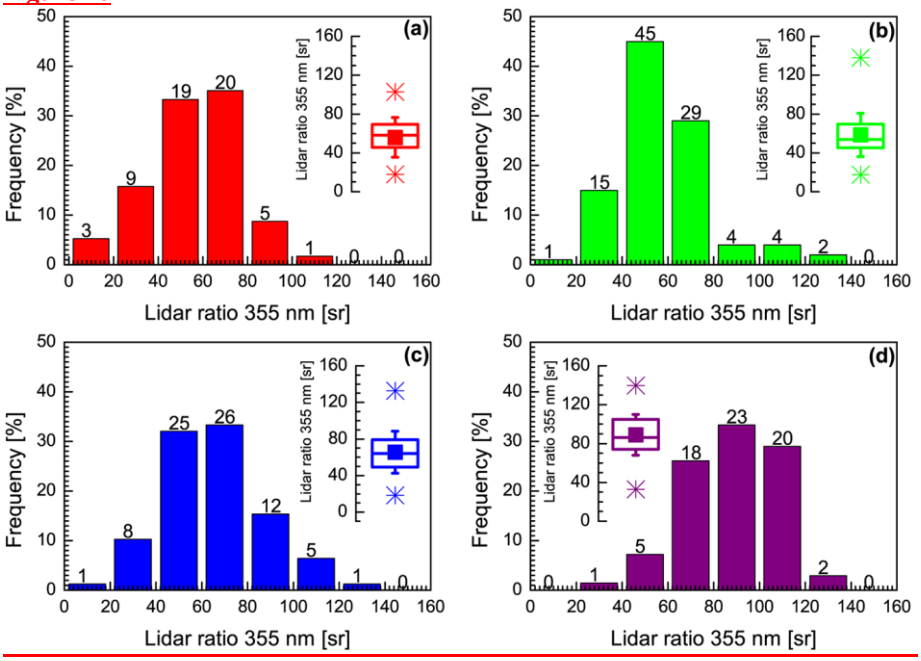
(a)
(b)
(c)
(d)
Frequency [%]
Lidar ratio 355 nm [sr]
Lidar ratio 355 nm [sr]
3
9
19
20
5
1
0
0
1
15
45
29
4
4
2
0
1
8
25
26
12
5
1
0
0
1
5
18
23
20
2
0

Figure 11